

# We are IntechOpen, the world's leading publisher of Open Access books Built by scientists, for scientists

6,900

Open access books available

186,000

International authors and editors

200M

Downloads

Our authors are among the

154

Countries delivered to

TOP 1%

most cited scientists

12.2%

Contributors from top 500 universities



WEB OF SCIENCE™

Selection of our books indexed in the Book Citation Index  
in Web of Science™ Core Collection (BKCI)

Interested in publishing with us?  
Contact [book.department@intechopen.com](mailto:book.department@intechopen.com)

Numbers displayed above are based on latest data collected.  
For more information visit [www.intechopen.com](http://www.intechopen.com)



---

# Raman Spectroscopy of Graphitic Nanomaterials

---

Daniel Casimir, Iman Ahmed, Raul Garcia-Sanchez,  
Prabhakar Misra and Fabiola Diaz

Additional information is available at the end of the chapter

<http://dx.doi.org/10.5772/intechopen.72769>

---

## Abstract

This chapter showcases some of the versatility of Raman spectroscopic data as applied to the characterization of single (SWNT) and multi-walled (MWNT) carbon nanotubes, few layer graphene and functionalized graphene nanoplatelets, with an emphasis on gas-sensing applications. Specifically, water vapor and a variety of toxic gases (NO, NO<sub>2</sub>, and SO<sub>2</sub> at 500 ppm in gaseous nitrogen) have been targeted for detection over the temperature range 24–200°C. The structure of sp<sup>2</sup>-hybridized carbon allotropes is reviewed and scanning electron microscopy (SEM) imagery utilized in conjunction with Raman spectroscopy to physically and spectrally characterize the various graphitic nanomaterials studied. A Kataura plot analysis associated with the Radial Breathing Mode (RBM) vibrations of SWNT has been used to identify possible chiralities in the graphitic samples employing 455, 532 and 780 nm laser excitation wavelengths to record the Raman spectra. The effect of temperature on the various Raman vibrational modes (RBM, G<sup>+</sup> and G<sup>-</sup>) has been investigated, along with a determination of the thermal conductivity of SWNT samples and correlation between the purity of the sample and the variation of the slope of the G<sup>+</sup> band with increasing laser power.

**Keywords:** Raman spectroscopy, carbon nanotubes, graphene, graphene nanoplatelets, nanomaterials

---

## 1. Introduction

The first class of materials whose properties and characterization via Raman spectroscopy we discuss here are the graphitic allotropes—single and multi-walled carbon nanotubes (SWNT, MWNT), followed by graphene and graphene nano flakes, specifically plasma functionalized graphene nanoplatelets. The chapter will begin with some discussion of the rich Raman spectral features of sp<sup>2</sup> carbon allotropes, which will be necessary since there will be an emphasis on

those particular Raman bands and features that provide useful structural/thermal data about carbon nanotube samples. It will be followed by an overview of graphene and graphene nanoplatelets and their usefulness for gas-sensing applications utilizing Raman spectroscopy.

The one-dimensional graphite allotrope, carbon nanotube, is conceptually described as being a rolled-up graphene sheet, yielding the cylindrical nanomaterials that have diameters of a few nanometers. The multi-walled varieties contain several concentric cylindrical shells. The Raman bands and the variations under various external perturbations of the  $sp^2$  graphitic materials cited above include the graphite G-band common to all  $sp^2$  carbons at around  $1580\text{ cm}^{-1}$  due to the intraplanar bond stretching of the two carbons in the hexagonal lattice unit cell, and the carbon nanotube specific radial breathing mode (RBM)—which arises as a consequence of their cylindrical geometry. Lastly, there is the defect D-Raman band, which arises due to defects, finite size effects, or any other cause of departure from perfect crystalline regularity, and the 2-D band. The characterization topics discussed in connection with the graphitic materials will be the identification of the chirality types present in carbon nanotube samples using the resonant RBM mode of carbon nanotubes and its connection to the interesting quasi 1-dimensional character of their electronic structure. The other properties obtained via Raman spectroscopy discussed will also be the anomalous thermal expansion and thermal conductivity of the  $sp^2$  graphitic materials investigated.

We have also utilized Raman spectroscopy to understand the behavior of vibrational modes associated with graphene following gas exposure. Specifically, we have studied the effects of water vapor and toxic gases ( $\text{SO}_2$ ,  $\text{NO}_2$ ,  $\text{NO}$ ), via variable humidity levels, gas concentrations, exposure times, and thermal loading, on the Raman spectra of graphene.

Functionalized graphene nanoplatelets are comprised of an amorphous mixture of graphene sheets. Their thicknesses range from 6 to 8 nm, and the overall density usually lies between 0.03 and 0.1 g/cc. The oxygen content of the majority of samples normally are  $<1\%$ , with the remaining carbon content exceeding 99.5 wt % (STREM). The morphology of this amorphous material plays a large and significant role in its enhanced mechanical properties, such as stiffness, strength, and surface hardness. By incorporating a small number of certain atoms that differ in the number of valence electrons into the pure crystal, the doping of graphene nanoparticles can lead to an enhancement in conductivity.

For the thermal conductivity measurements of the carbon allotropes, we have used the G-Raman band and its variation with increased sample temperature through laser heating. The method and the useful information it provides is due to Terekhov et al. [1]. Also, edge defect characterization of graphene nanoplatelets based on Eq. (1) due to Cancado et al. [2] has also been included, where  $L$  is the characteristic in-plane crystallite size of the graphene nano flake,  $\lambda$  is the laser wavelength, and  $I_D$  and  $I_G$  are the intensities of the Raman D-band and G-band, respectively.

$$L = (2.4 \times 10^{-10}) \times \lambda^4 (I_D/I_G)^{-1} \quad (1)$$

Our research presented here is aimed at extending the knowledge regarding the nature of graphitic nanomaterial-gas sensing interactions and help develop better models for their enhanced understanding, which in turn would make the development and production of more effective *in situ* gas sensors feasible.

## 2. Structure of $sp^2$ nanocarbons

This introductory section presents a cursory discussion of SWNT and MWNT structures. This will be done by first looking at the unit cell of planar graphene and also graphite since the former material is considered to be the conceptual parent material of all  $sp^2$  graphitic materials, including SWNTs through the application of a simple rolling up operation. Since the molecular/electronic and geometric structures are highly dependent on graphene, the majority of a SWNT's structural features are expressed via the lattice vectors  $\vec{a}_1$ , and  $\vec{a}_2$  of the graphene unit cell shown in **Figure 1**.

The two unique Carbon atoms A and B in each unit cell are located respectively at  $(0, 0)$  and at  $1/3 * (\vec{a}_1 + \vec{a}_2)$  (**Figure 1** adapted from Wong and Akinwande [3]). The progression to the first related graphitic material, three dimensional graphite, is accomplished through the stacking of several layers of 2-dimensional graphene layers, where in the A-B Bernal stacking structure, there are  $2 * N$  atoms per unit cell,  $N$  being the number of layers [4]. A major structural factor of graphite that results in the electronic structure of 2-dimensional graphene being a reasonable first order approximation of the former is the average inter-layer spacing of 3.35 Angstroms. This distance is much larger than the nearest neighbor Carbon–Carbon distance of 1.42 Å, hence resulting in much weaker overall attractive interaction between layers compared to intra-planar interactions [5].

Moving now to one of major foci of the chapter single-walled carbon nanotubes (SWNTs), the conceptual operation performed on the single 2-dimensional graphene sheet is “rolling” it up into a cylinder. The diameter distribution of most SWNTs produced by various techniques is dominated by tubes with diameters less than 2 nm, although diameters in the range of 0.7–10.0 nm are possible [5]. Ignoring the two ends and exploiting the very large length to diameter ratio ( $\sim 10^4$ – $10^5$ ) of SWNTs allows one to safely view these  $sp^2$  nanocarbons as quasi 1-dimensional objects [5].

The concept of chirality is essential in the description of SWNT structure. It is defined by the chiral vector, denoted by  $C_h$  in **Figure 1**, and several equivalent interpretations of this structural quantity are usually given. For example one may consider the fact that the chiral vector determines the arrangement of the six-sided carbon hexagons in the curved planar wall of the SWNT [5]. Alternatively, one may also view the chirality of a SWNT in terms of the overall symmetry of the constructed SWNT, specifically whether or not the SWNT has vertical mirror plane reflection

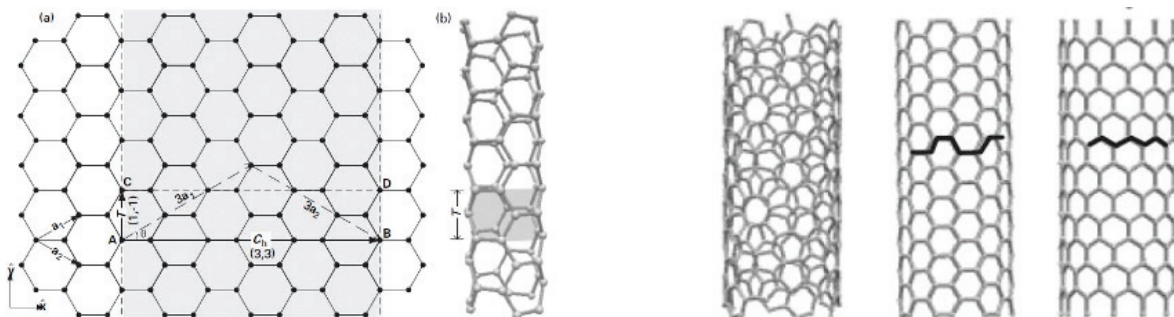


**Figure 1.** Graphene unit cell.

symmetry across planes containing the tube axis [3]. An additional benefit of the latter viewpoint is its more direct path to the discovery of there being only three overall structural categories of SWNT as shown in **Figure 1**.

Chiral SWNTs are formed such that the orientation of the carbon hexagons on the tube surface do not allow the sides of the tube across a vertical mirror plane to be superimposed on one another. The remaining two subcategories achiral SWNTs, armchair and zig-zag SWNTs however, do allow for such reflection symmetry based on the arrangement of the Carbon hexagons along the cylinder walls. The names armchair and zig-zag refer to the circular cross-sections of each of these achiral SWNT types shown by the bold lines in **Figure 1**. We conclude this section dealing with the structural properties of primarily SWNTs with the actual construction of a SWNT, starting just the two SWNT graphene lattice vectors,  $\vec{a}_1$  and  $\vec{a}_2$ , which have the following Cartesian components  $\left[\frac{a\sqrt{3}}{2}, \frac{a}{2}\right]$ , and  $\left[\frac{a\sqrt{3}}{2}, -\frac{a}{2}\right]$  respectively.

Relying on the example of **Figure 1** which demonstrates the formation of a (3, 3) armchair nanotube, the planar unit cell is formed by rolling the gray shaded region along the chiral vector such that points C and D coincide respectively with points D and B. After performing the previous conceptual rolling operation the pertinent quantity that defines the SWNT unit cell in the resultant nanotube is the translational vector  $\vec{T}$  as shown in the right hand portion of **Figure 1**. As its name suggests this vector is the shortest vector that is perpendicular to the chiral vector, and represents the axial component of the SWNT unit cell that is repeated in this same direction. This formalism of SWNT construction that begins from the planar graphene lattice provides the readily obvious interpretation for the magnitude of the chiral vector, namely its magnitude equaling the nanotube circumference given by the expression,  $|\vec{C}_h| = a\sqrt{m^2 + n^2 + nm}$  where  $a \approx 2.46 \text{ \AA}$  is the graphene hexagonal lattice constant equal to  $\sqrt{3}$  times the nearest neighbor C-C distance of  $1.42 \text{ \AA}$ . The remaining structural parameter in **Figure 1**, the angle  $q$ , is the chiral angle, conventionally chosen to be the angle between the chiral vector and the  $\vec{a}_1$  lattice vector. This angle ranges from  $0^\circ \leq q \leq 30^\circ$  with the lower bound corresponding to zig-zag SWNTs and the upper bound corresponding to armchair SWNTs. The integers,  $n$  and  $m$  simply refer to the number of  $\vec{a}_1$  and  $\vec{a}_2$  lattice vectors used in the construction of the chiral vector usually with the convention of  $n \geq m$ . For zig-zag SWNTs  $m = 0$ , and in the case of armchair SWNTs both chiral indices are identical [3].

### 3. Experimental

In Raman spectroscopy, a laser diode emits photons, which interacts with the sample, most of the light bouncing off unchanged with the same frequency as the source (Rayleigh scattering). However, a small amount of light experiences an energy shift (Raman scattering) and is filtered to allow only the Raman scattered light to be collected by the detector. The sample vibrates uniquely to its structure and each vibration mode uniquely alters the emitted photons wavelength and that change is graphed as intensity per wavelength. An unknown sample's Raman spectrum can be compared to the known Raman spectral graph.

### 3.1. Thermo fisher scientific DXR smart Raman spectrometer

The primary instrument used to record the majority of the Raman spectra was a DXR SmartRaman spectrometer (that uses 780, 532, and 455 nm laser sources). The first wavelength (780 nm) was used for the bulk of the recorded spectra and utilized a high brightness laser of the single mode diode (as does the 532 nm light source), while the 455 nm source is a diode-pumped solid state laser. This instrument employs the 180-degree backscattering geometry, full range grating and triplet spectrograph, coupled with automated entrance slit selections in order to provide the Stokes-shifted Raman bands.

### 3.2. Renishaw inVia Raman spectrometer

The Renishaw inVia Raman spectrometer uses a 532-nm laser source and was used to obtain the Stokes spectra of the graphene and functionalized Nanoplatelets samples. It consists of a microscope to shine light on the sample and collecting the scattered light, filtering all the light except for the tiny fraction that has been Raman scattered, together with a diffraction grating for splitting the Raman scattered light into component wavelengths, and a CCD camera for final detection of the Raman spectrum.

### 3.3. Ventacon heated cell

The Raman spectral data in this study of the two different SWNT samples were obtained under thermal loading from room temperature to 200°C in steps of 10°C. Both powdered samples were heated externally via a Ventacon™ model H4–200 heat cell that is diagrammed in **Figure 2**. The first SWNT sample was produced by Unidym™ Carbon Nanotubes. The Hipco technique was used in the production of this sample, which involves the nucleation of SWNTs on Fe(CO)<sub>5</sub> catalyst material using high pressure CO, followed by various quality control methods (Misra et al., 2013) [6]. According to manufacturer specifications, the diameters and lengths of the nanotubes in this sample ranged between 0.8 to 1.2 nm, and 100 to 1000 nm, respectively. The sample data also claimed a purity level of only 8% residual Fe catalyst by weight present.

Information about the method of production or purity levels of the second SWNT sample was not available. In the data sets for both samples each point in the  $\omega_{\text{RBM}}$  vs. temperature plots is the mean value from two separate Raman collections. The standard error of each data point obtained from both Raman spectra collected at each temperature is also displayed for both samples. The spectra recorded at each pre-set temperature were obtained with a temperature variation of  $\pm 0.1^\circ\text{C}$ .

### 3.4. Aluminum disk cell for graphene gas exposure Raman spectroscopy

**Figure 3** is a diagram of the components of the sample cell and how it is placed underneath the Renishaw Raman spectrometer. The cell contains apertures that connect to the center of the cell, where the sample is placed and sealed through means of a glass disk and an O-ring. In addition, the cell has an aperture to place a thermocouple to read the temperature of the cell and another one where we place a voltage-induced heating cylinder. The gas flow comes from the gas cylinder into the rotameter and then through a series of tubing to the cell. These tubes

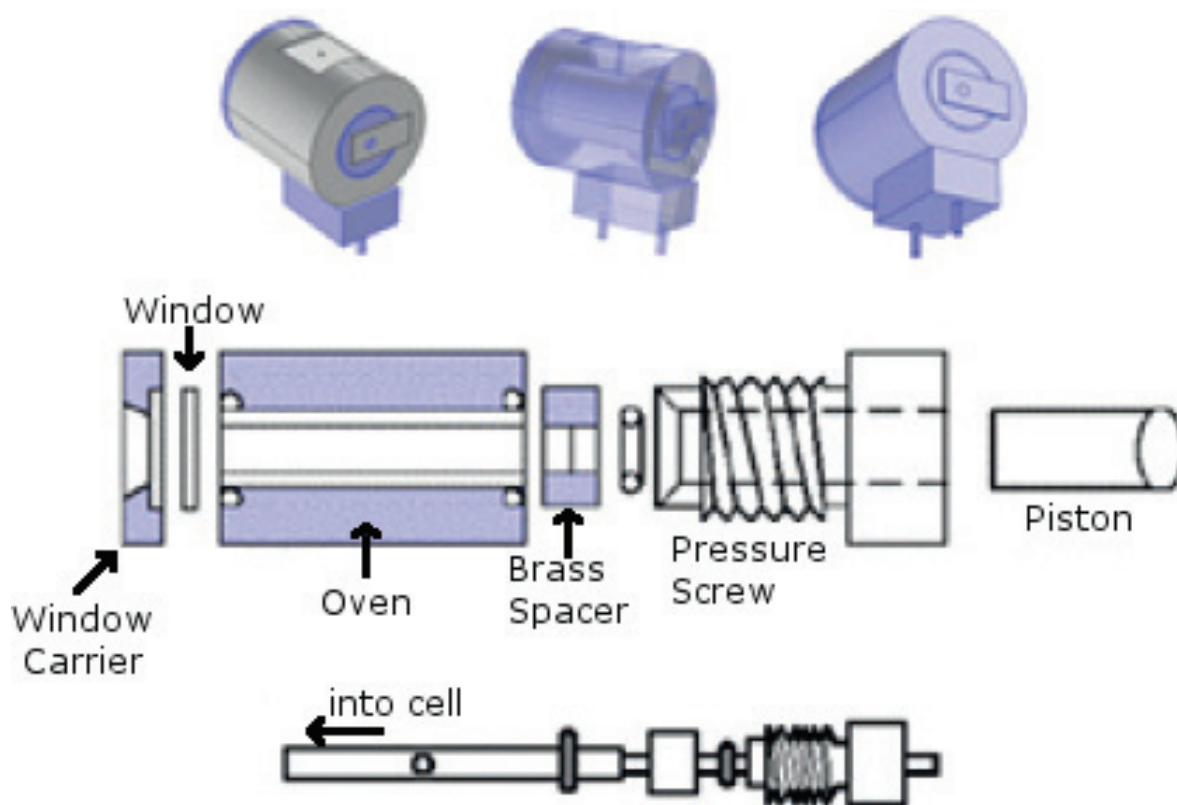


**Figure 2.** Top: Ventacon H4-200 heat cell. Middle: Cross sectional layout of oven. Bottom: Cylindrical powdered/solid sample holder.

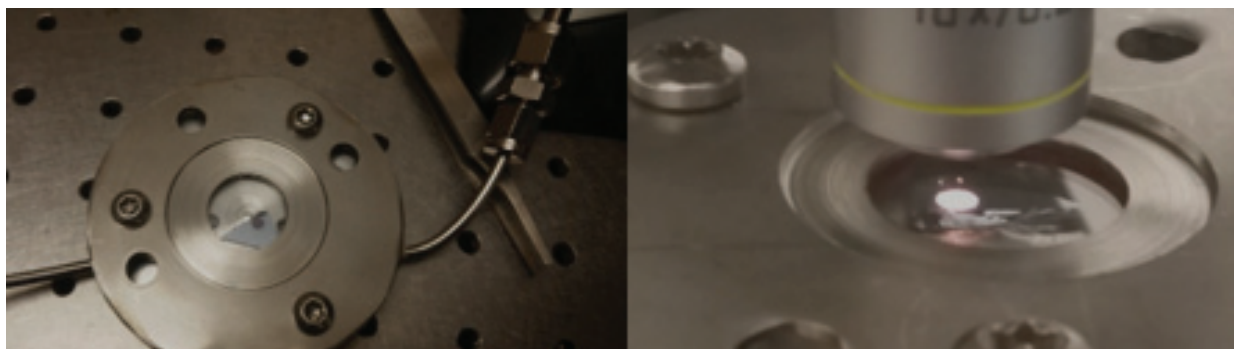


**Figure 3.** Aluminum disk cell used for gathering Raman spectral data during gas exposure of graphene samples; top view (left) | under Raman microscope (right) [7].

connect to holes within the sealed sample chamber and flow out through the other output tube and into the bubbler. The bubbler is submerged in liquid nitrogen in order to separate the more dangerous components of the gases used and flow the rest through an inlet fan connected to an exhaust. At the end of the experiment, the bubbler is placed in a fume hood and left until the following day. **Figure 4** shows multiple components of this setup that were used for the gas exposure experiments.

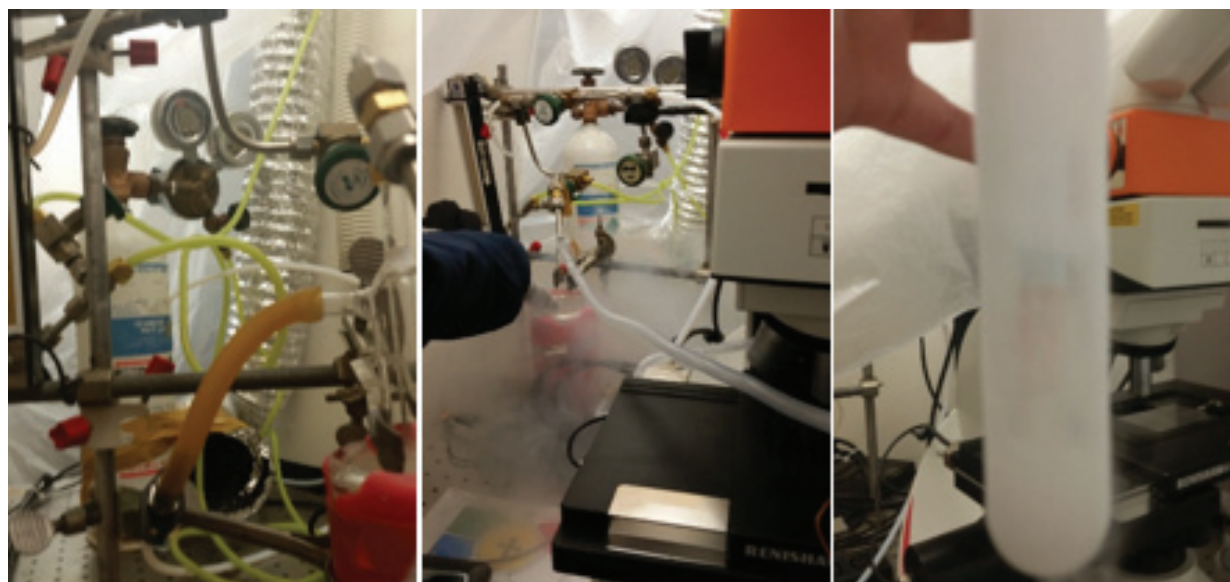


**Figure 4.** Left: Setup showing the tubing layout for the gas exposure Raman spectroscopy experiments; center: Filling the bubbler with liquid nitrogen to break up dangerous gas components; right: Bubbler after experiments had concluded [7].

The measurement sequence for the gas exposure of graphene samples is as follows:

1. The sample is placed in the cell, nitrogen gas flows into the sample chamber and heated up to the 130–150°C temperature range. Raman spectroscopy data are taken as the cell heats up. Typically, 60 scans are taken, with a 20-second exposure for graphene. The voltage is adjusted in order to control the temperature increase.
2. Voltage is reduced and the Raman spectral data recorded, as the temperature drops back to near ambient value.
3. Nitrogen flow stops and the toxic gas for that experiment flows into the sample chamber. We take sets of 120 exposures with laser exposure and delays that result in a 30-minute exposure. This is repeated for different gas flows, with the rotameter reading 50, 100, 150 and maximum values for a total of 2-hour exposure.
4. We repeat Steps 1 and 2 to see if the Raman features return back to normal; this allows us to verify the effects of the gas exposure on the graphene sample.

### 3.5. JEOL JSM-7600F scanning electron microscope

Images of functionalized graphene nanoplatelets were taken with the JEOL JSM-7600F scanning electron microscope [8]. The secondary electron detector on the SEM uses an EMI current of 138.20 nA. Beam current has a range of 1 pA to 200 nA. The JEOL JSM-7600F SEM contains a large variety of detectors that can be used on specimen samples up to 200 mm in diameter. Various magnifications were selected when appropriate to accurately display the sample structure; SEM magnifications range between 25 and 1000000×. The modular software program Gwyddion was used to generate 3-dimensional visualization of the nanoplatelet aggregate structures.

#### 4. Raman spectra of single-walled carbon nanotubes (SWNTs)

The current section is an overview of the Raman active modes of SWNTs. The current treatment is meant only to preview the Raman bands and features relied on most heavily during the authors' characterization of SWNT samples. The first of the Raman bands featured in this section is the G-band, so called since it is common to all  $sp^2$  nanocarbons, centered at  $\sim 1580 \text{ cm}^{-1}$ . This high energy band is a consequence of the in-plane C-C bond stretching. Interestingly due to the induced strain from the curvature of SWNT walls the G-band for these structures is split into several peaks, with the two most prominent ones being the symmetric  $A_1$  denoted as  $G^+$  and  $G^-$  at  $\sim 1590$  and  $\sim 1560 \text{ cm}^{-1}$ , respectively. The variation of the smaller of these two peaks with diameter is given by [4]:

$$\omega_G = 1591 + \frac{C}{d_t^2} \quad (2)$$

where  $d_t$  is the nanotube diameter, and the value  $C$  corresponding to the  $G^-$  band for semi-conducting and metallic nanotubes respectively are  $47.7$  and  $79.5 \text{ cm}^{-1} \text{ nm}$ . The above relation is derivable solely from a careful application of elasticity theory to SWNTs [4]. The later discussion of the use of the temperature variation of the  $G^+$  band in connection with thermal conductivity is based on a time-dependent perturbation of the  $G^+$  Raman band.

Next, the Raman band at around  $1300\text{--}1350 \text{ cm}^{-1}$  is the D-Band, which has been shown in [9] to be associated with any defects or departures from perfect regularity in the  $sp^2$  graphite lattice. Equation (3) shows the variation of typical crystallite sizes  $L_a$  with the Raman laser excitation energy, and ratio of the intensity of the D-band and G-band, based on a more recent version of Tuinstra and Koenig's original analysis [9]:

$$L_a(nm) = \left( \frac{560}{E_{laser}^4} \right) \left( \frac{I_D}{I_G} \right)^{-1} \quad (3)$$

The final Raman band featured in this section, the radial breathing mode is only present carbon nanotube spectra, and is therefore used as an indication of their presence in  $sp^2$  Carbon samples. As implied by its name the intra-planar displacement of the C-atoms in this Raman active mode is effectively in the radial direction of the resultant SWNT, as if the entire SWNT is breathing. There are two significant features associated with this particular SWNT Raman band in connection with their structural and electronic properties. The first is the inverse relationship between the RBM frequency and SWNT diameter expressed in Eq. (4):

$$\omega_{RBM} = \frac{A}{d_t} \quad (4)$$

Similar to Eq. (1) this relation is also based on continuum elasticity theory. Since the original work done on this relationship was based on individual SWNTs of the kind typically produced via the super-growth method, further work by various groups led to Eq. (5), which is an extension of the prior equation that accounts for environmental perturbations of the RBM, especially on SWNTs in macroscopic bundled samples [4]:

$$\omega_{RBM} = \frac{227}{d_t} \sqrt{1 + C_e d_t^2} \quad (5)$$

The overall environmental contribution to the RBM shift is contained in the fitted constant  $C_e$ , which is unique to SWNTs produced by any of the various available techniques. In the case of SWNTs produced by the HiPCO technique used in our studies,  $C_e$  was determined to have a value of 0.05 [4].

The second critical feature associated with the RBM band is its role in expressing the link between the quasi 1-dimensional electronic behavior and structure of SWNTs. The phenomenon referred to above is the resonant character of the Raman spectra of SWNTs, in which the intensity of Raman scattering from a SWNT is increased many fold when the laser excitation energy is very near that of an optical transition. **Figure 5** shows the density of states for a representative metallic and semi-conducting single-walled carbon nanotube, respectively, and

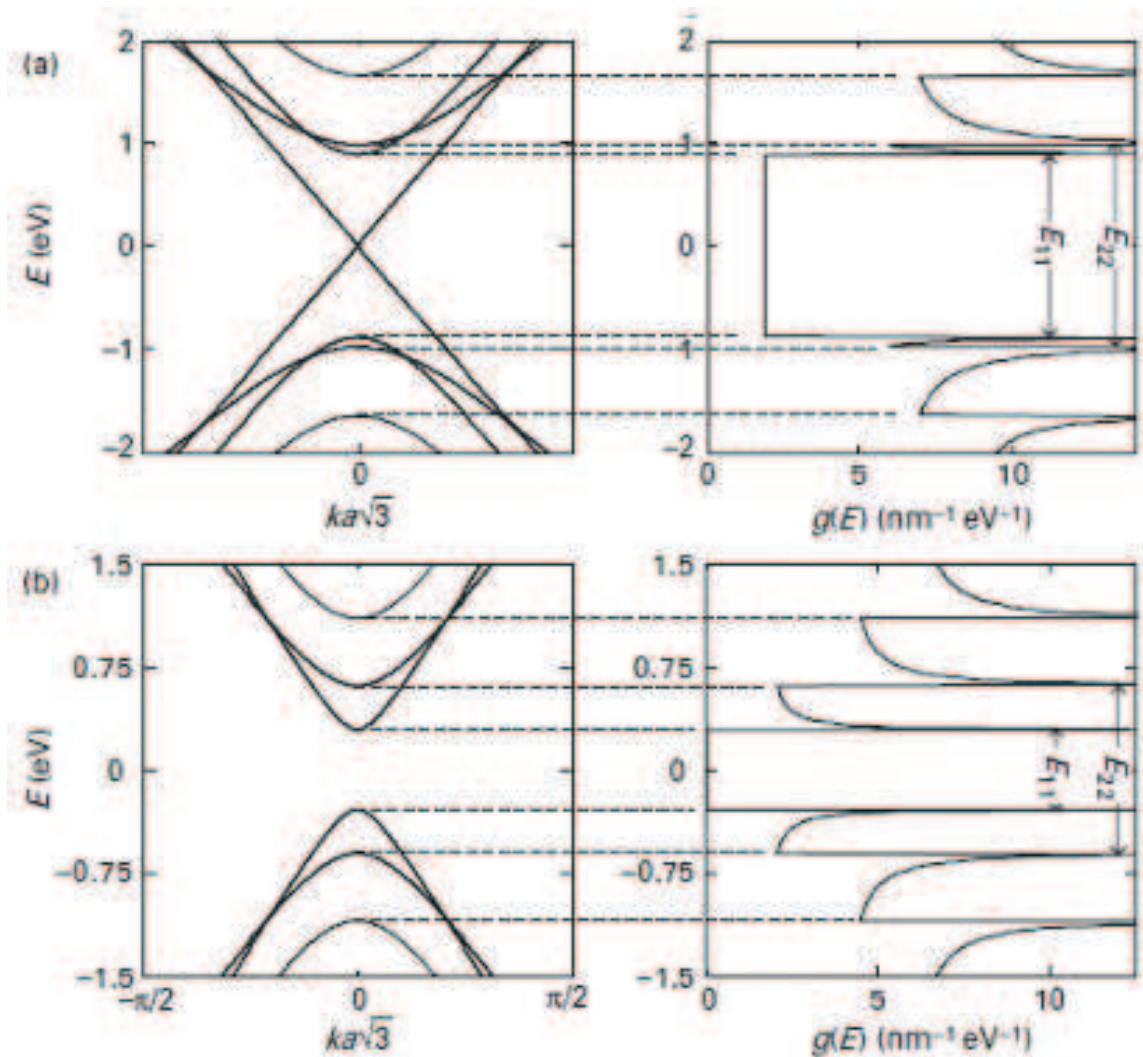


**Figure 5.** Electronic density of states for a metallic and semi-conducting SWNT shows two transitions labeled,  $E_{11}$  and  $E_{22}$ , between the corresponding valence and conduction bands.

shows two such transitions, labeled  $E_{11}$  and  $E_{22}$ , between the corresponding valence and conduction bands (adapted from [3]).

These sharp divergences between the optical transitions are known as van Hove singularities. Such singularities arise from the form of the density of states expression for a 1-dimensional sample as indicated in Eq. (6), which is derived for the simple free electron gas model [3]:

$$g(E) = \begin{cases} \frac{1}{h} \sqrt{\frac{2m}{E - E_0}}, & E > E_0 \\ 0, & E \leq E_0 \end{cases} \quad (6)$$

The density of states of the electrons and holes in SWNTs shows the two most significant characteristics of Eq. (6), namely the inverse square root variation with energy, and the van Hove divergences at energies close to the Fermi level  $E_0$ . Kataura [4] made arguably one of the most significant contributions to both the theoretical description and practical use of these resonance Raman effects with the introduction of the so-called Kataura Plot in 1999. These plots of nanotube diameter or RBM frequency vs. optical transition energy  $E_{ii}$ , which are now in common use for the identification of the chiralities present in a SWNT sample, are possible due to the  $E_{ii}$  values' inverse dependence to SWNT diameter. The use of a theoretically derived Kataura plot for  $(n, m)$  identification begins the following section discussing our actual use of Raman spectral data in SWNT sample characterization.

## 5. Raman spectral SWNT characterization

### 5.1. Kataura plot analysis

The discussion of Section 4 means that in Raman spectra from bundled SWNTs, which is the case in this research, the majority of the signal comes from those tubes in the sample with diameters that are resonant with the excitation wavelength [4]. Therefore, this makes Kataura plots extremely useful in identifying the possible chiral indices contained in any SWNT samples one may be working with. Displayed in **Figures 6–8**, and **Table 1**, are the theoretical Kataura plots and Raman spectral data that were used to identify the chiralities present in one of the SWCNT samples used in the present study.

### 5.2. Thermal expansion

In this section, we discuss the effect of temperature on the Raman vibrational modes of SWNTs and subsequent use of this valuable effect in obtaining an estimate of the thermal expansion for one of the SWNT samples used in the present study [10].

Considering the phonon frequency  $\omega(V, T)$  as a function of volume  $V$ , and temperature  $T$ , the derivatives of this quantity with respect to pressure and volume can be connected to each other via the equations

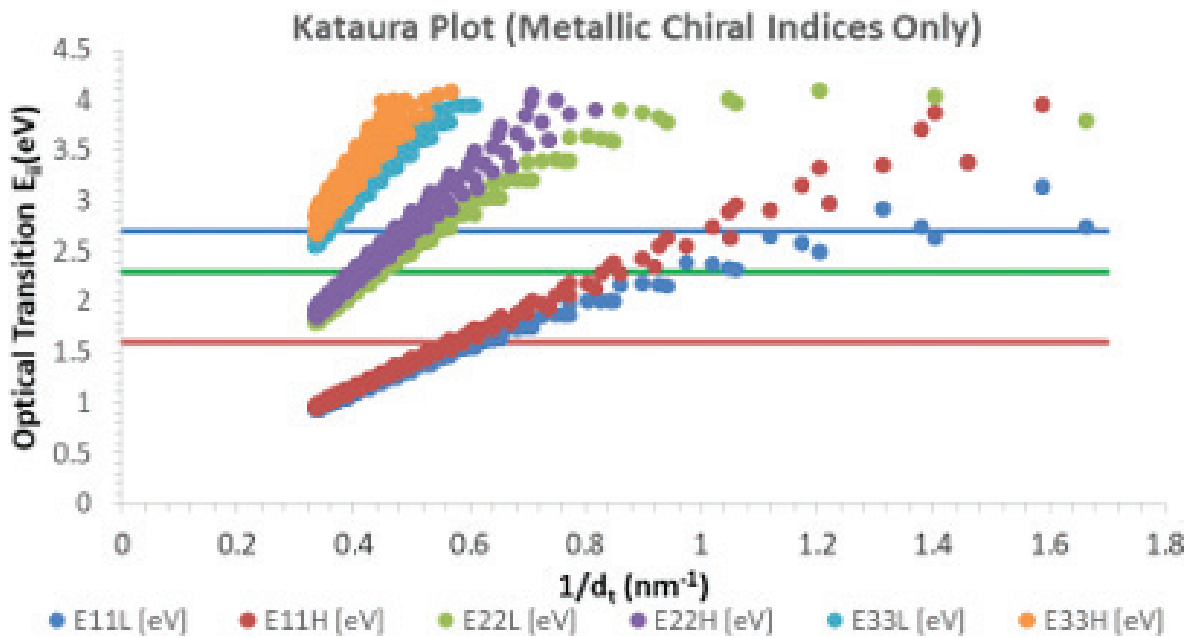


**Figure 6.** Theoretical Kataura plot for metallic SWNTs. The three horizontal lines from top to bottom represent respectively, the 455, 532, and 780 nm laser excitation wavelengths used on the SWNT sample. The intersection of the horizontal lines with the Kataura plot at any of the diameters obtained from the radial breathing modes help to identify possible chiralities in the sample. The Kataura plot data was obtained from K. Saito, et al. [5].

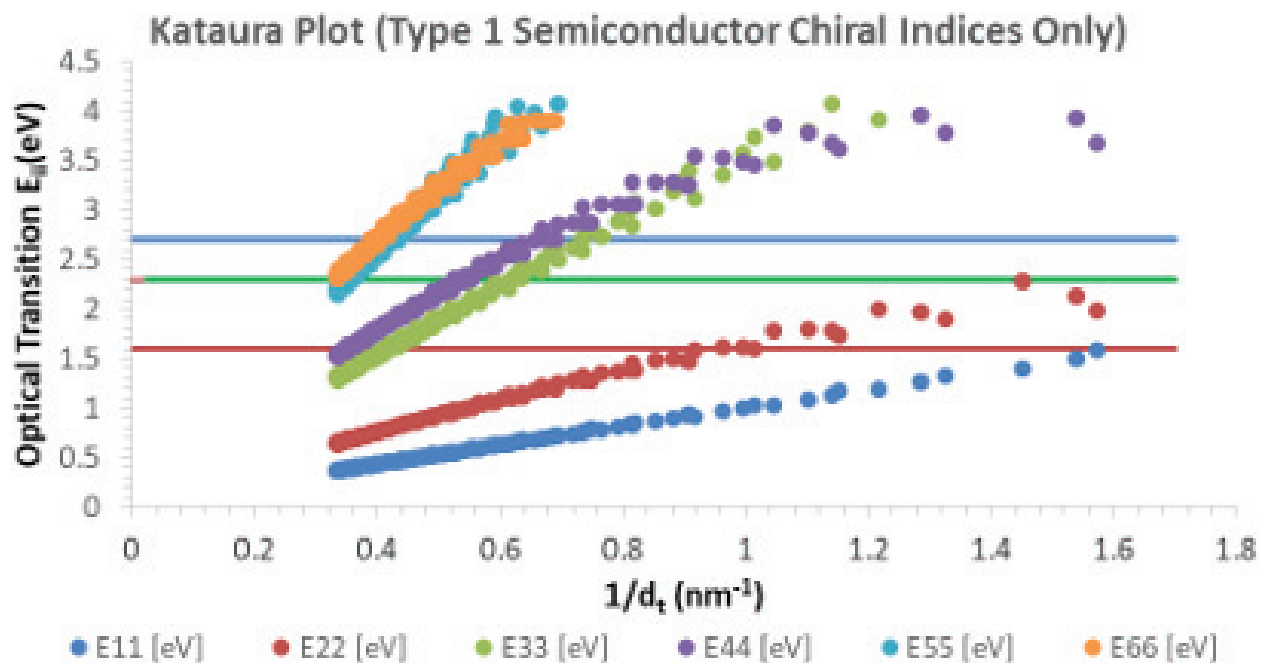


**Figure 7.** Theoretical Kataura plot for type 1 semi conducting SWNTs. The three horizontal lines from top to bottom represent respectively, the 455, 532, and 780 nm laser excitation wavelengths used on the SWNT sample. The intersection of the horizontal lines with the Kataura plot at any of the diameters obtained from the radial breathing modes help to identify possible chiralities in the sample. The Kataura plot data was obtained from Saito et al. [5].

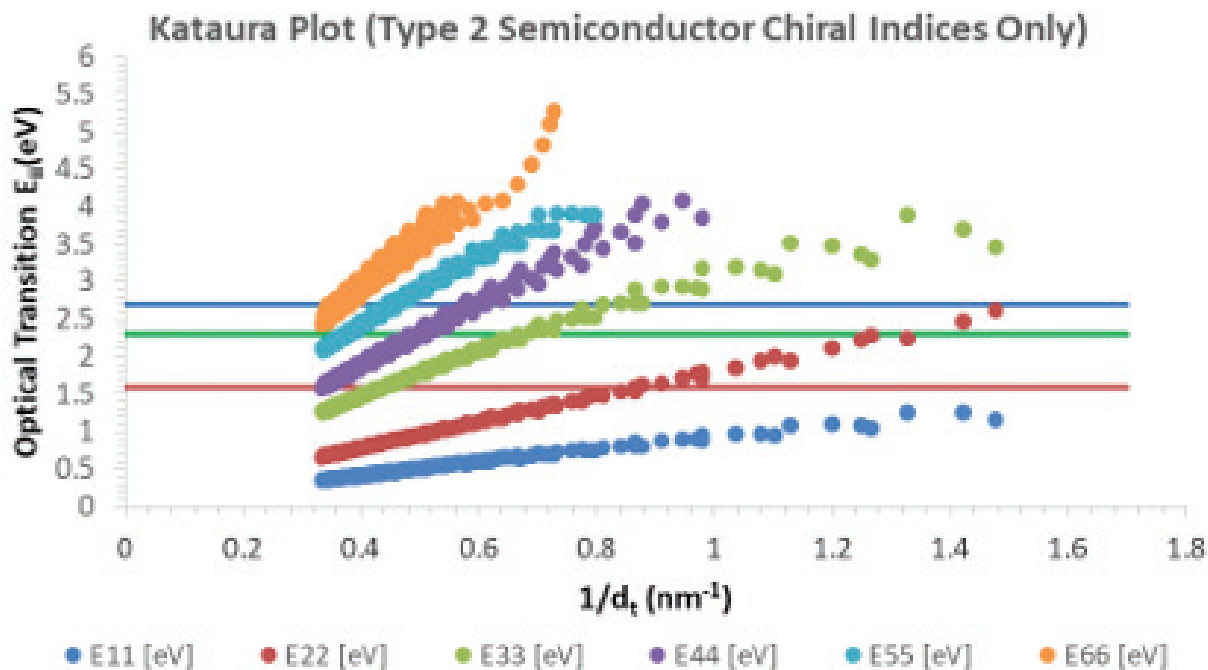


**Figure 8.** Theoretical Kataura plot for type 2 semi conducting SWNTs. The three horizontal lines from top to bottom represent respectively, the 455, 532, and 780 nm laser excitation wavelengths used on the SWNT sample. The intersection of the horizontal lines with the Kataura plot at any of the diameters obtained from the radial breathing modes help to identify possible chiralities in the sample. The Kataura plot data was obtained from Saito et al. [5].

(1) Laser Excitation (nm)	Radial Breathing Mode (cm <sup>-1</sup> )	$1/d_t$ (nm <sup>-1</sup> )	Resonant Chiralities
780	150.51	0.632	(12,12), (20,2), (17,5), (16,7)
532	166.04	0.697	***†
455	171.57	0.721	***†
(2) Laser Excitation (nm)	Radial Breathing Mode (cm <sup>-1</sup> )	$1/d_t$ (nm <sup>-1</sup> )	Resonant Chiralities
780	150.51	0.632	***†
532	166.04	0.697	***†
455	171.57	0.721	(15,4), (17,3), (18,1)
(3) Laser Excitation (nm)	Radial Breathing Mode (cm <sup>-1</sup> )	$1/d_t$ (nm <sup>-1</sup> )	Resonant Chiralities
780	150.51	0.632	***†
532	166.04	0.697	(14,7), (15,5), (16,3), (17,1)
455	171.57	0.721	***†
†No resonant SWCNTs			

**Table 1.** Identification of metal type, type 1 semiconducting and type 2 semiconducting chiral indices in SWNT samples using Kataura plots.

$$\left(\frac{\partial\omega}{\partial V}\right)_T = \left(\frac{\partial\omega}{\partial P}\right)_T \left(\frac{\partial P}{\partial V}\right)_T \quad (7)$$

and

$$\left(\frac{\partial\omega}{\partial V}\right)_T = -\left(\frac{B_T}{V}\right)_T \left(\frac{\partial\omega}{\partial P}\right)_T \quad (8)$$

where  $B_T$  is the isothermal bulk modulus which equals  $B_T = -V\left(\frac{\partial P}{\partial V}\right)_T$  [11]. Next, a connection between the temperature derivatives at fixed volume and pressure are obtained by writing

$$d\omega = \left(\frac{\partial\omega}{\partial V}\right)_T dV + \left(\frac{\partial\omega}{\partial T}\right)_V dT \quad (9)$$

which after dividing through by  $dT$  at constant pressure yields

$$\left(\frac{\partial\omega}{\partial T}\right)_P = \left(\frac{\partial\omega}{\partial T}\right)_V + \left(\frac{\partial V}{\partial T}\right)_P \left(\frac{\partial\omega}{\partial V}\right)_T \quad (10)$$

Equation (10) gives a breakdown of the measurable temperature variation of the phonon frequency on the left in terms of two contributions. The first term on the right represents the intrinsic, purely thermal contribution to the lowering of the phonon frequency caused by the anharmonic intermixing of the various phonon modes [12]. The second term, often referred to as the “pure volume” effect, represents the induced phonon shift to lower frequency with temperature due to a reduction in the bonds’ force constants brought about by typical volume increases with temperature, namely thermal expansion.

The laser excitation wavelength used to obtain the Raman data for the purified Hipco produced sample was 780 nm with a 6 mW power setting. Some other collection parameters associated with this sample were an exposure time of 10.0 s during each of the 3 exposures for each recorded Raman spectrum. Lastly, the aperture setting used for the entrance slit was a 25-micron slit.

Similarly, for the second SWNT sample, the laser power setting for the heated Raman spectra was 6 mW, but this time with 532 nm excitation. A larger entrance slit aperture, 50 microns in width was used, in addition to the exposure time and number of exposures for the Raman spectra at each temperature being 10.0 s and 6 respectively. It must be noted that there is an unexpected “kink” or change in slope in **Figures 9** and **10** at approximately 350 K temperature for all of the Raman bands. This phenomenon which is more noticeable in **Figure 9** for the purified Hipco sample requires further examination.

**Figures 9** and **10** show the results of our reproduction [10] of the linear downshift of the primary first order Raman frequencies with temperature for two SWNT samples, along with each sample’s corresponding Scanning Electron Microscopy (SEM) images. The linearity of

this trend is due to the dominance of the “purely temperature” effect’s contribution over that of the contribution from thermal expansion as was noted in [13] and [14], where the latter authors were able to separate each of the two contributions’ effects on graphite.

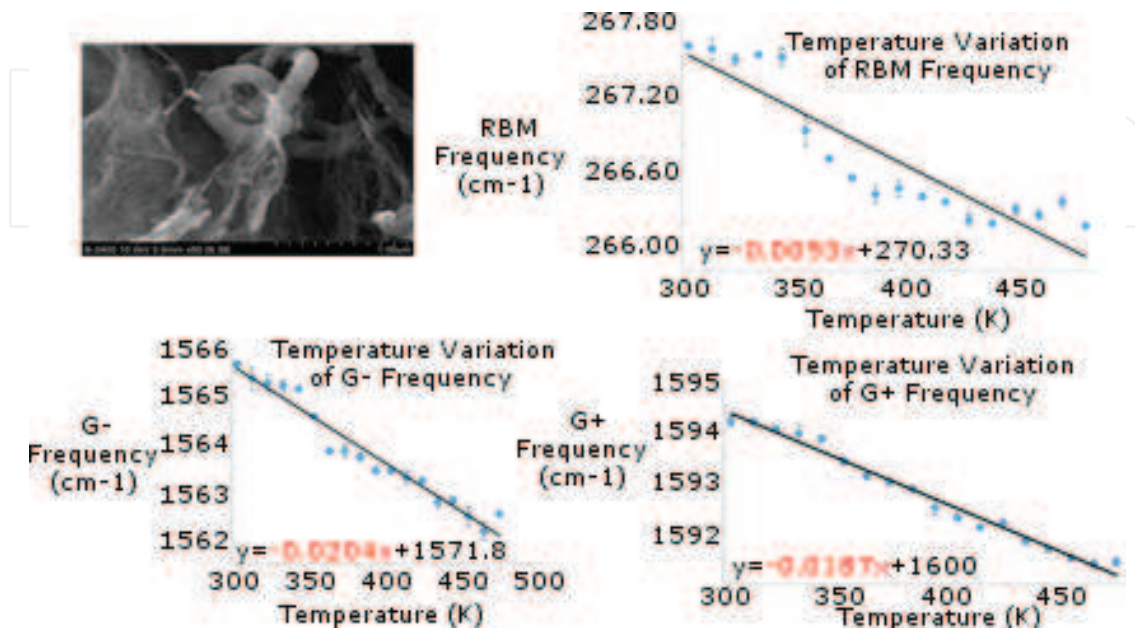


**Figure 9.** Top left: Scanning electron microscopy (SEM) image of HipCO produced SWNT sample; top right: Variation with temperature of the first order RBM vibration; bottom left: G<sup>-</sup> Raman band and bottom right: G<sup>+</sup> Raman band of a SWNT sample heated externally with the Ventacon heat cell. A 780-nm wavelength laser excitation was used for recording the Raman spectra on this HipCO produced sample.

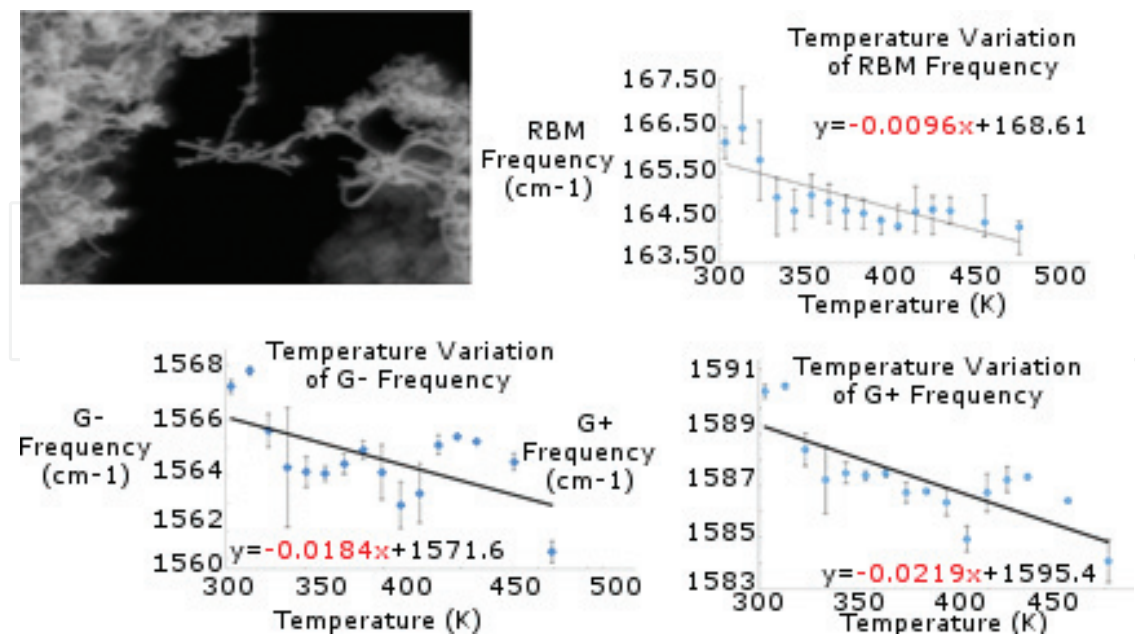


**Figure 10.** SEM image of SWNT sample (top left); temperature variation of the first order Raman RBM (top right), G<sup>-</sup> band (bottom left), and G<sup>+</sup> band (bottom right), with temperature of a SWNT sample heated externally with the Ventacon heat cell. 532 nm laser excitation was used for recording the Raman spectra.

The temperature effect dominance of the phonon frequency downshift mentioned above also manifests itself in the empirical polynomials usually used to express experimental data associated with this phenomenon, such as the example in Eq. (11):

$$\omega(T) = \omega_0 + a_1T + a_2T^2 \quad (11)$$

In the reported values of the temperature redshift of Raman frequencies throughout the literature the second-order term  $a_2$  is often negligible compared to its first order counterpart  $a_1$ , resulting in a primarily linear trend that was caused mainly by thermal effects not associated with volumetric changes as discussed above.

We now present our results of the use of Resonant Raman Spectroscopy to determine the volume coefficient of thermal expansion (CTE) behavior of the second SWNT sample obtained through the use of the temperature shifted radial breathing mode band. The technique used to determine the volume CTE  $\beta$ , is the same as that used by Espinosa-Vega et al. [15]. **Figure 11** shows the variation with temperature of the fractional volume change of the resonant SWNTs associated with the sole radial breathing mode band of  $166.0 \text{ cm}^{-1}$  that was present in our spectra. The resulting volume thermal expansion coefficient  $\beta$ , and the same results from [15] are also displayed in **Figure 11**. Based on the premise of the bundled SWNTs being arranged in the sample as circular cylinders of equal length, which was the same assumption made by Espinosa-Vega et al. [15], we obtained the volume at each temperature using the previously discussed relationship between  $\omega_{\text{RBM}}$  and tube diameter:

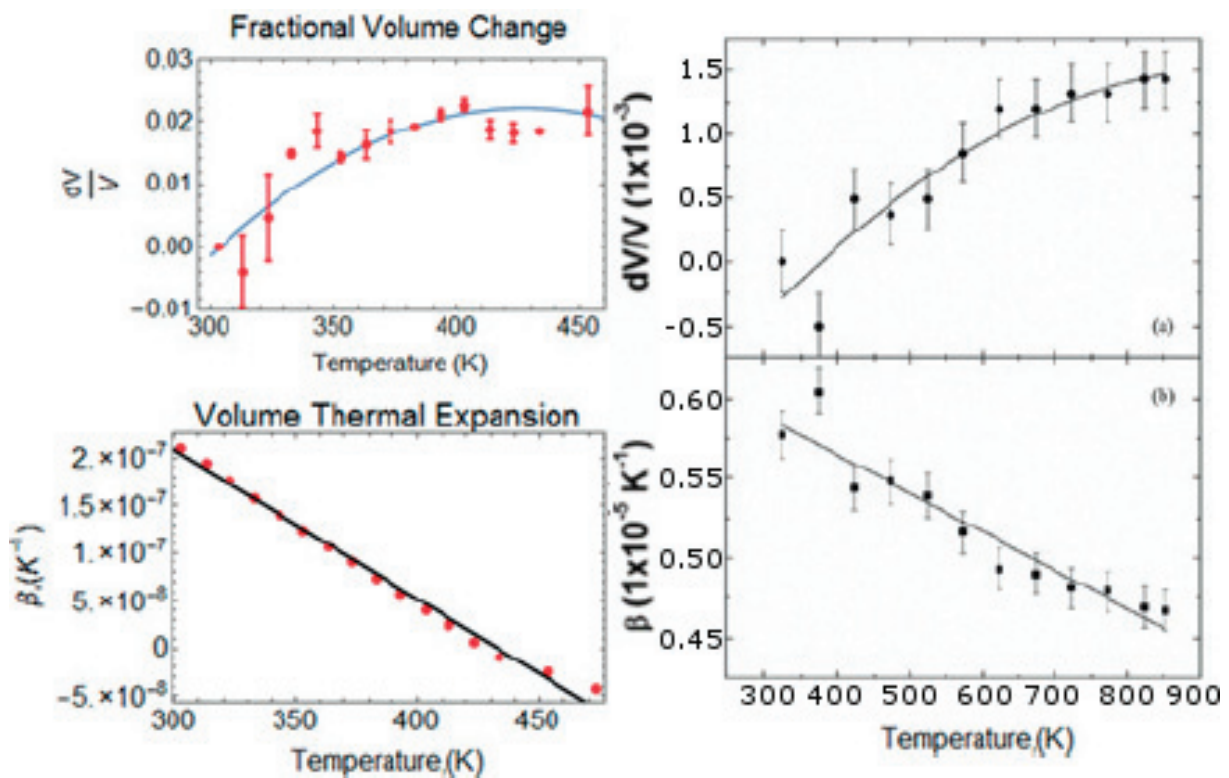


**Figure 11.** Temperature variation of the fractional change in volume and the volume thermal expansion obtained from the radial breathing mode Raman band (left). Corresponding data are from Espinosa-Vega et al. [15] (right).

$$\omega_{RBM} = \frac{A}{d_t} + B \quad (12)$$

The respective values for A and B of  $248.0 \text{ cm}^{-1}\cdot\text{nm}$  and  $10.0 \text{ cm}^{-1}$  were used by Espinosa-Vega et al. [15].

The linear temperature dependence of the volume coefficient of thermal expansion (CTE)  $\beta$  was then obtained as shown in **Figure 11** with Espinosa-Vega's data on the right for comparison. According to [12], both the fractional volume data and subsequent linear trend in  $\beta$  led to the conclusion that the temperature dependence of the volume varied as  $e^{c+bt+aT^2}$ . The resulting values for the parameters a, b, and c from our model were  $-1.46 \times 10^{-6}$ ,  $0.00125142$ , and  $-0.245$  respectively. The linear downshift in the data for  $\beta$  goes from  $0.2 \times 10^{-6}$  to  $-0.5 \times 10^{-7} \text{ K}^{-1}$ , with a slope of  $-1.6 \times 10^{-9} \text{ K}^{-2}$ , over the experimental temperature range of  $\sim 300\text{--}473 \text{ K}$ . Espinosa-Vega et al.'s data show  $\beta$  decreasing from  $5.8 \times 10^{-6}$  to  $4.7 \times 10^{-6} \text{ K}^{-1}$  over a larger temperature range of  $300\text{--}875 \text{ K}$  [15].

Espinosa-Vega et al.'s Raman spectra were obtained in a nitrogen atmosphere, whereas ours were collected under open air ambient conditions. This is why the Espinosa-Vega experiment was allowed to operate at the very high (maximum) temperature of  $875 \text{ K}$  before the onset of any irreversible changes to the Raman spectrum frequencies, such as the loss of intensity brought about by the thermal deterioration of the SWNTs. The smaller values of the temperature slope values  $\Delta\omega/\Delta T$  obtained in the nitrogen atmosphere, as opposed to in open air, also meant that Espinosa-Vega et al.'s SWCNTs had a greater thermal stability [15].

Another possible reason for Espinosa-Vega et al.'s  $\beta$  values being much greater than ours was that their experiment was performed on SWNT samples at a much lower density, possibly even at the individual level, due to the pre-processing they performed on their samples. They initially formed a dispersion of their SWNTs with benzene, which was then annealed on a Silicon surface before any Raman spectra were done. The Raman measurements in the present study, however, were all performed on macroscopic bundled samples where van der Waals interactions among the individual tubes were a significant factor. Espinosa-Vega et al. also provided data on the linear decrease of the volume CTE for SWNTs in ambient air, which ranged from  $3.3 \times 10^{-6}$  to  $2.7 \times 10^{-6} \text{ K}^{-1}$  again over the operating temperature range of  $300\text{--}875 \text{ K}$ . Although, their volume CTE values are still larger, the decrease from their values associated with their experiments done in a nitrogen atmosphere support our earlier suggestion of our lower values of  $\beta(T)$  being due in part to the lower thermal stability of the SWNTs under ambient air conditions.

### 5.3. Thermal conductivity

We conclude this section dealing with SWNT properties of interest obtainable via Resonant Raman spectroscopy, with a discussion on obtaining an estimate of sample thermal conductivity. The method used was developed by Terekhov et al. [1], who show that there is a demonstrable correlation between the slope of the variation of the  $G^+$  Raman band with increasing laser power at the sample spot for SWNT samples containing different percentages of true

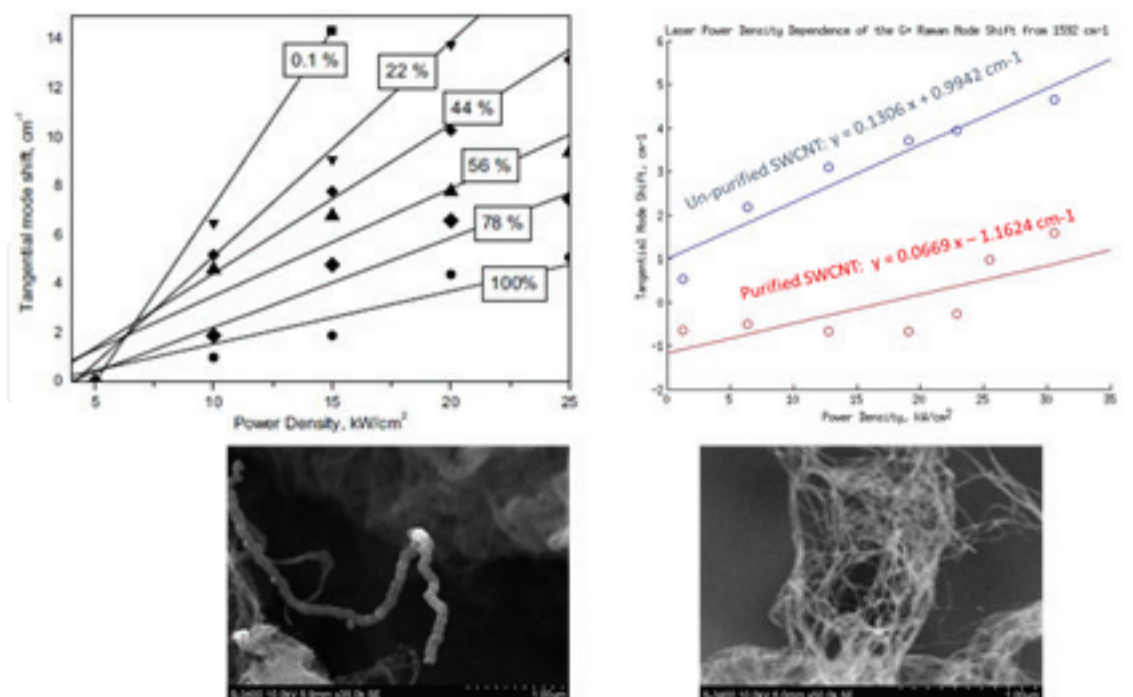


**Figure 12.** Variation of the  $G^+$  Raman band of SWNT samples of differing purity levels. (top left) data from Terekhov, S.V., et al., AIP Conference Proceedings, (685), 2003, where the percentages indicate the estimated amount of actual carbon nanotubes present in the sample. (Top right) Our data for the two SWNT samples imaged below. The higher purity HiPCO SWNT sample on the left contains ~8% residual catalyst material.

SWNT content. In other words, the slope depends on sample “purity,” where samples with less purity exhibit larger/steeper slope variations in contrast with high purity samples composed almost entirely of SWNTs. Since additional analysis performed by Terekhov et al. [1] also show that the slope rate of change of the  $G^+$  band with increased laser power is inversely proportional to thermal conductivity  $\kappa$ , using this method allows one to estimate the thermal conductivity of a SWNT sample by simply taking the ratio of the experimentally determined slope variation and an accepted literature value of the thermal conductivity of amorphous Graphite. **Figure 12** shows our reproduction of the above described effect on two SWNT samples (also pictured in the figure) of differing purity, with the less pure sample indeed exhibiting a greater rate of decline of the Raman  $G^+$  band with increased laser power at the sample spot.

## 6. Temperature and gas exposure effects on graphene Raman spectra

The Raman spectra of graphene were also recorded at varying temperatures (30–200°C) using the Ventacon heated cell and the 780-nm laser with the DXR Raman spectrometer. The graphene samples were all on a silicon/SiO<sub>2</sub> substrate and subjected to consecutive heating/cooling cycles between 30 and 200°C in a sealed chamber. **Figure 13** is the spectrum collected at 30°C. As discussed earlier, the G-band at 1598 cm<sup>-1</sup> originates from intraplanar stretching, while the peak at 2703 cm<sup>-1</sup> corresponds to the 2D band. The latter band is due to a second-order two-phonon process that is highly dispersive. It was discovered that this band can be

used in estimating the number of layers of a graphene sample. Based on the analysis for this study, the graphene sample(s) in this experiment proved to be largely single-layered. A third band around  $3078\text{ cm}^{-1}$  was also present among the Raman spectra collected. It was tracked

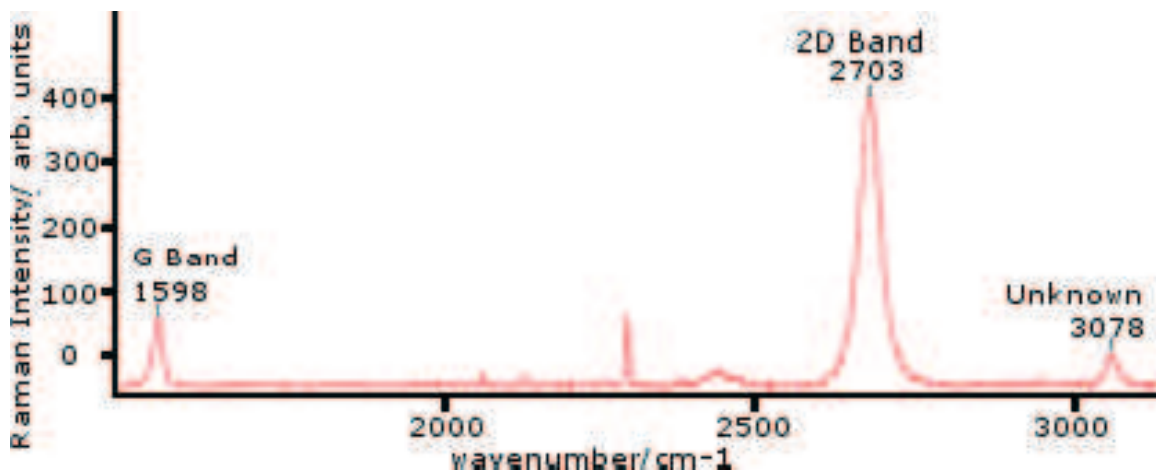


Figure 13. Raman spectrum of graphene at  $30^\circ\text{C}$ .

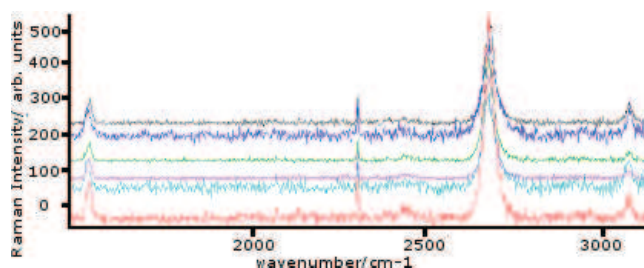


Figure 14. Raman spectra illustrating the sensing of water vapor and humidity effects on graphene as a function of temperature in the range  $24.0\text{--}150.0^\circ\text{C}$  [top to bottom: Sample at  $24.0^\circ\text{C}$  (pristine graphene before heating/pre-exposure),  $150.5^\circ\text{C}$  (after heating/pre-exposure),  $29.3^\circ\text{C}$  (after cooling/pre-exposure),  $26.4^\circ\text{C}$  (last of gas exposure),  $149.0^\circ\text{C}$  (after heating/post-exposure), and  $28.5^\circ\text{C}$  (after cooling/post-exposure, respectively)].

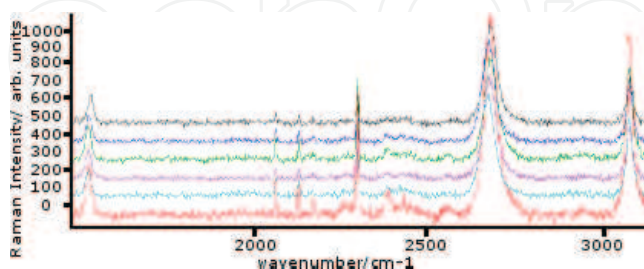


Figure 15. Raman spectra illustrating the sensing of NO gas on graphene as a function of temperature in the range  $24.0\text{--}150.0^\circ\text{C}$ . [top to bottom: Sample at  $24.8^\circ\text{C}$  (pristine graphene before heating/pre-exposure),  $139.2^\circ\text{C}$  (after heating/pre-exposure),  $27.7^\circ\text{C}$  (after cooling/pre-exposure),  $27.5^\circ\text{C}$  (last of gas exposure),  $146.2^\circ\text{C}$  (after heating/post-exposure), and  $28.9^\circ\text{C}$  (after cooling/post-exposure, respectively)].

and is probably due to the substrate or glass surface of the microscope stage. Another possibility is that it is either an overtone Raman band of graphene or a C-H stretch benzene ring vibration. Further analysis is needed to determine with certainty the precise origin of the spectral feature at  $3078\text{ cm}^{-1}$ .

Raman spectra of the graphene sample(s), under similar heating/cooling cycles was also performed simultaneously with exposure to gaseous ( $\text{H}_2\text{O}$ ,  $\text{NO}$ ,  $\text{SO}_2$ ,  $\text{NO}_2$ ). This analysis allowed us to search for any possible patterns in the response of the graphene as its temperature was increased before gas exposure. Each Raman spectral acquisition was analyzed with regards to band frequency, band intensity, and peak width.

Plots of the Raman shift, light intensity, and peak width vs. temperature (in the range  $30\text{--}150^\circ\text{C}$ ) were recorded before exposure and after being exposed to a specific gas. These plots (**Figures 14–17**) were made for all four vapor and gases of interest ( $\text{H}_2\text{O}$ ,  $\text{NO}$ ,  $\text{SO}_2$ ,  $\text{NO}_2$ ).

The plots of the Raman shift, light intensity, and peak width over the temperature range  $24.0\text{--}150^\circ\text{C}$  before and after being exposed to  $\text{NO}$  are shown in **Figure 18** [16].

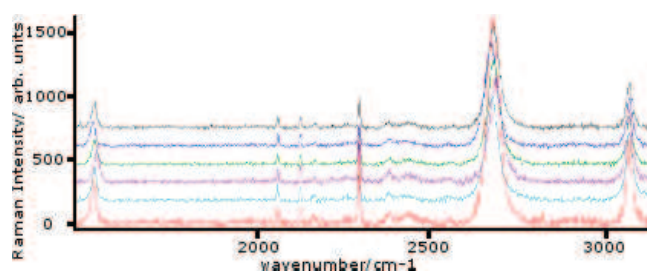


**Figure 16.** Raman spectra illustrating the sensing of  $\text{NO}_2$  gas on graphene as a function of temperature in the range  $26.0\text{--}150.0^\circ\text{C}$ . [top to bottom: Sample at  $26.2^\circ\text{C}$  (pristine graphene before heating/pre-exposure),  $151.2^\circ\text{C}$  (after heating/pre-exposure),  $31.4^\circ\text{C}$  (after cooling/pre-exposure),  $28.9^\circ\text{C}$  (last of gas exposure),  $150.0^\circ\text{C}$  (after heating/post-exposure), and  $32.4^\circ\text{C}$  (after cooling/post-exposure, respectively)].

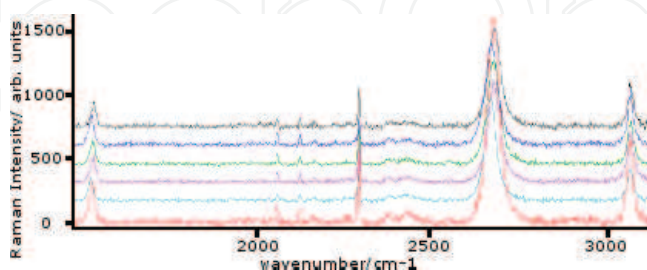


**Figure 17.** Raman spectra illustrating the sensing of  $\text{SO}_2$  gas on graphene as a function of temperature in the range  $24.0\text{--}137.0^\circ\text{C}$ . [top to bottom: Sample at  $24.3^\circ\text{C}$  (pristine graphene before heating/pre-exposure),  $149.0^\circ\text{C}$  (after heating/pre-exposure),  $29.3^\circ\text{C}$  (after cooling/pre-exposure),  $27.7^\circ\text{C}$  (last of gas exposure),  $135.6^\circ\text{C}$  (after heating/post-exposure), and  $31.1^\circ\text{C}$  (after cooling/post-exposure, respectively)].

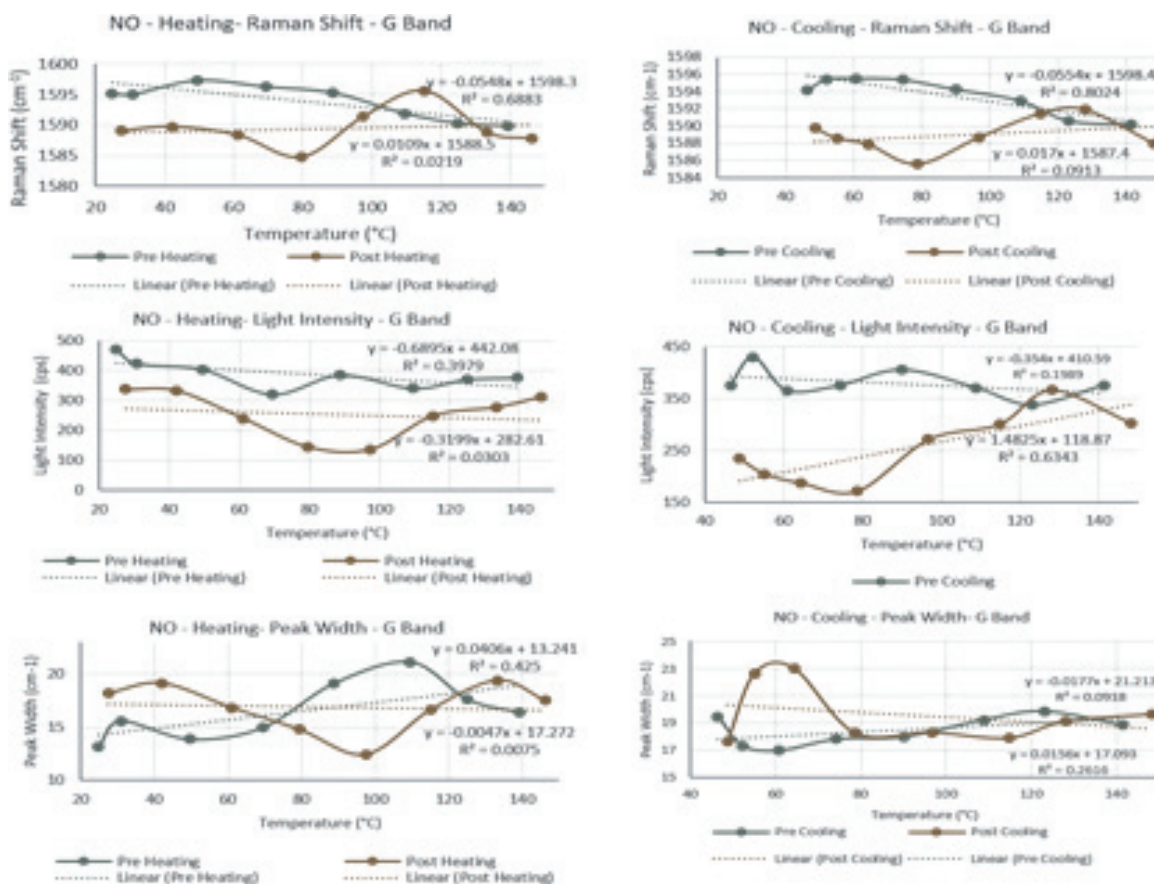


Figure 18. Plots showing the change in Raman frequency shift, light intensity, and peak width, over a temperature range (30–150°C), before and after being exposed to NO [16].

## 7. Physical properties and Raman spectra of graphene Nanoplatelets

All of the graphene nanoplatelet samples investigated in the current study (functionalized oxygen, nitrogen, argon, ammonia, carboxyl and fluorocarbon) have similar shapes (see Table 2 and Figure 19) [17]. Graphene nanoplatelet aggregates (aggregates of sub-micron platelets with diameters of <2 microns and a thickness of a few nanometers) were identified and studied, rather than individual nanoplatelets (STEM Data Sheets) [18].

The electronic structure of graphitic nanocarbons is linked to its structure, and Raman spectroscopy is sensitive to this intimate and unique relationship, which makes it very effective at studying the various functionalized graphene nanoplatelets used in this study. Akin to pristine

Functional species	X average (μm)	Y average (μm)	Z average (μm)
Argon	4.8	3.9	0.50
Carboxyl	4.3	4.5	0.57
Oxygen	4.7	4.3	0.90
Ammonia	4.4	3.7	0.64
Fluorocarbon	5.0	3.6	0.55
Nitrogen	6.7	6.5	0.91

Table 2. Average x, y, z axis spatial measurements of functionalized graphene nanoplatelet aggregates.

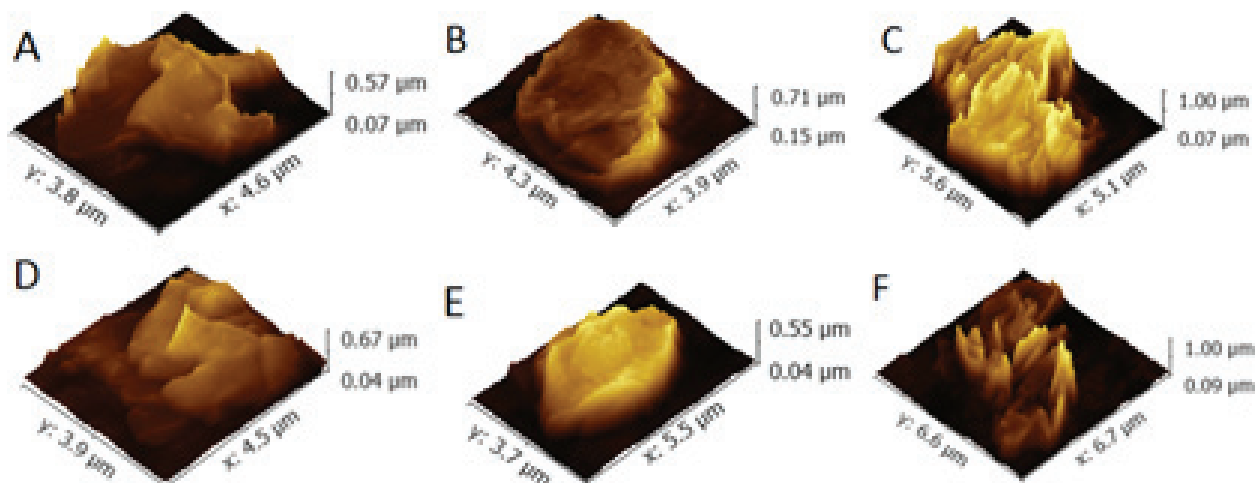


**Figure 19.** 3D view of SEM data of functionalized graphene nanoplatelet aggregates doped with argon (a), carboxyl (b), oxygen (c), ammonia (d), fluorocarbon (e), and nitrogen (f) via Gwyddion software [19].

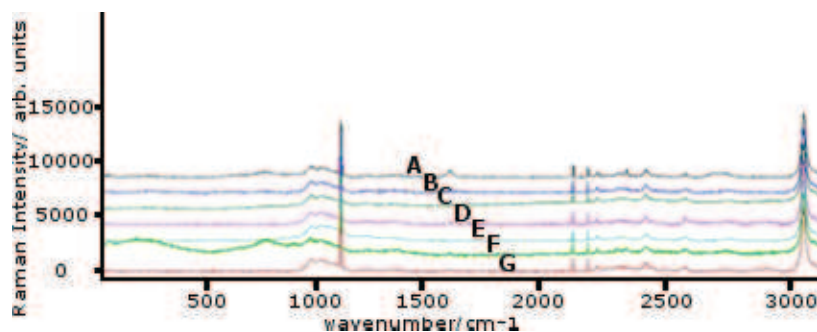


**Figure 20.** Offset Raman measurements of CVD graphene (a), functionalized graphene nanoplatelet aggregates doped with ammonia (b), argon (c), carboxyl (d), fluorocarbon (e), nitrogen (f), and oxygen (g) at room temperature ( $\sim 25^\circ\text{C}$ ) displayed using the Renishaw's WiRE software [21].

graphene, the Raman spectra are characterized by the G and 2D bands. The D band present in the spectra signaled some defects. The behavior of the sharp Lorentzian G-band, at  $1587\text{ cm}^{-1}$ , can also be used to verify the sample layer thickness. An increase in the number of layers lowers the frequency of this band, along with an increase in peak intensity. The 2D band, however, depends on the band position and shape, exhibiting distinct band shape differences with the numbers of layers present (AZO Materials) [20]. **Figure 20** indicates identical position and shape of G and 2D bands visible in the spectra of the CVD graphene and the functionalized graphene nanoplatelet samples at room temperature ( $\sim 25^\circ\text{C}$ ).

## 8. Conclusions and outlook

The thermal characteristics of a variety of graphitic nanomaterials (single-walled and multi-walled carbon nanotubes, graphene and functionalized graphene in the form of nanoplatelets) have been investigated in the temperature range  $24.0\text{--}200^\circ\text{C}$  using Raman spectroscopy for enhanced gas-sensing and optoelectronic applications. A Kataura plot analysis has been presented for the Radial Breathing Mode vibrations of single-walled carbon nanotubes and possible chiralities identified that pertain to metallic, semiconductor and type 2 semiconducting SWNTs. The effect

of temperature on the Raman vibrational modes (RBM,  $G^+$  and  $G^-$  bands) of SWNTs has been investigated and the thermal expansion of the SWNT sample determined. A demonstrable correlation between the slope of the variation of the  $G^+$  Raman band with laser power for varying levels of SWNT purity has been obtained showing clearly that less pure samples exhibit a steeper slope variation with enhanced laser power. We have also investigated in some detail the behavior of Raman vibrational modes of graphene as a function of temperature in the range (24–150°C), following exposure to a variety of toxic gases (NO, NO<sub>2</sub> and SO<sub>2</sub>) at 500 ppm concentration in nitrogen with an eye toward developing sensitive chemical and biological sensors that are efficient, sensitive and portable.

## Acknowledgements

Financial support from the National Science Foundation (Award No. PHY1659224) *REU Site in Physics at Howard University* is gratefully acknowledged.

## Author details

Daniel Casimir<sup>1</sup>, Iman Ahmed<sup>1</sup>, Raul Garcia-Sanchez<sup>1</sup>, Prabhakar Misra<sup>1\*</sup> and Fabiola Diaz<sup>2</sup>

\*Address all correspondence to: pmisra@howard.edu

1 Laser Spectroscopy Laboratory, Department of Physics and Astronomy, Howard University, Washington, DC, USA

2 Department of Physics and Astronomy, Francis Marion University, Florence, SC, USA

## References

- [1] Terekhov SV, Obraztsova ED, DetlaffWeglikowska U, Roth S. Calibration of Raman based method for estimation of carbon nanotube purity. In: Proceedings of the XVII International Winterschool/Euroconference on Electronic Properties of Novel Materials; 8-15 March 2003; Austria. pp. 116-119
- [2] Cancado LG, Jorio A, Pimenta MA. Measuring the absolute Raman cross section of nanographites as a function of laser energy and crystallite size. *Physical Review B*. 2007;**76**. DOI: 10.1103/PhysRevB.76.064304
- [3] Wong HSP, Akinwande D. *Carbon Nanotube and Graphene Device Physics*. New York: Cambridge University Press; 2011. 251 p. DOI: 10.1017/CBO9780511778124
- [4] Jorio A, Dresselhaus G, Dresselhaus MS, editors. *Carbon Nanotubes: Advanced Topics in the Synthesis, Structure, Properties and Applications*. 1st ed. Springer; 2008. 709 p. DOI: 10.1007/978-3-540-72865-8
- [5] Saito R, Dresselhaus G, Dresselhaus MS, editors. *Physical Properties of Carbon Nanotubes*. 1st ed. London: Imperial College Press; 1998. 259 p

- [6] Misra P, Casimir D, Garcia-Sanchez R. Thermal Expansion Properties of Single Walled Carbon Nanotubes, by Raman Spectroscopy at 780nm Wavelength. Annual International Conference on Optoelectronics Photonics and Applied Physics (OPAP). 2013. pp. 52-55
- [7] Garcia-Sanchez R. Characterization of Metal Oxide Gas Sensors Materials Using Raman Spectroscopy and Computer Simulations. Washington, DC: Howard University; 2015
- [8] Scanning Electron Microscope JEOL JSM – 7600F [Internet]. Available from: [http://www.sfr.st.keio.ac.jp/forms/FE-SEM-J\\_manual\\_in\\_EN.pdf](http://www.sfr.st.keio.ac.jp/forms/FE-SEM-J_manual_in_EN.pdf) [Accessed: 2017-10-06]
- [9] Tuinstra F, Koenig JL. Raman Spectrum of graphite. *The Journal of Chemical Physics*. 1970;**53**:1126-1130. DOI: 10.1063/1.1674108
- [10] Casimir D. Investigation of Thermal Expansion Properties of Single Walled Carbon Nanotubes by Raman Spectroscopy and Molecular Dynamics Simulation. Washington, DC: Howard University; 2014
- [11] Wallace DC. *Thermodynamics of Crystals*. 1st ed. New York: Dover, 1998. 512 p
- [12] Calizo I, Balandin AA, Bao W, Miao F, Lau CN. Temperature dependence of the Raman spectra of graphene and graphene multilayers. *Nano Letters*. 2007;**7**:2645-2649. DOI: 10.1021/nl071033g
- [13] Dresselhaus MS, Eklund PC. Phonons in carbon nanotubes. *Advances in Physics*. 2000;**49**:705-814. DOI: 10.1080/000187300413184
- [14] Tan P, Deng Y, Zhao Q, Cheng W. The intrinsic temperature effect of the Raman spectra of graphite. *Applied Physics Letters*. 1999;**74**:1818-1820. DOI: 10.1063/1.123096
- [15] Espinosa-Vega LI, Rodriguez AG, Navarro-Contreras H, Vidal MA. Determination of the thermal expansion coefficient of Single-Wall carbon nanotubes by Raman spectroscopy. *Spectroscopy Letters*. 2013;**48**:139-143. DOI: 10.1080/00387010.2013.860172
- [16] Department of Physics and Astronomy: Research Experiences for Undergraduates in Physics, Diaz REU Research paper [Internet]. 2017. Available from: <http://physics1.howard.edu/REU/2017/Final/Fabiola%20Diaz%20Research%20Paper.docx> [Accessed: 2017-10-06]
- [17] Casimir D, Ahmed I, Garcia-Sanchez R, Misra P. Raman spectroscopy & scanning electron microscopy of carbon nanotubes, graphene & graphene nanoplatelets of relevance to energy storage & gas-sensing applications. In: *Proceedings of the International Conference on Computational & Experimental Engineering and Sciences (ICCES '17)*; 24-30 June 2017; Funchal, Madeira Island, Portugal: ICCES; pp. 484-487
- [18] Graphene Supermarket: HDPlas Graphene Nanoplatelets: Functionalized Graphene Nanoplatelet Trial Kit [Internet]. 2009. Available from: <https://graphene-supermarket.com/HDPlas-Graphene-Nanoplatelet-Trial-Kit.html> [Accessed: 2017-10-06]
- [19] Gwyddion – Free SPM (AFM, SNOM/NSOM, STM, MFM, ...) data analysis software [Internet]. 2004. Available from: [http://www.trichord-inc.com/pricing/frames/content/solar\\_power.pdf](http://www.trichord-inc.com/pricing/frames/content/solar_power.pdf) [Accessed: 2017-10-06]
- [20] Characterization of Graphene Using Raman Spectroscopy. AZO Materials. 2012. <http://www.azom.com/article.aspx?ArticleID=6271#3>
- [21] Renishaw WiRE Raman Software. 2001. Available from: <http://www.renishaw.com/en/raman-software-9450> [Accessed: 2017-10-06]

